Puttapaite, $Pb_2Mn^{2+}{}_2ZnCr^{3+}{}_4O_2(AsO_4)_4(OH)_6 \cdot 12H_2O$, a new mineral from the Beltana deposit, Puttapa, Flinders Ranges, South Australia, Australia.

Peter Elliott[1,2*] and Anthony R. Kampf[3]

[1]School of Physics, Chemistry and Earth Sciences, The University of Adelaide, Adelaide, South Australia 5005, Australia.

[2]South Australian Museum, North Terrace, Adelaide, South Australia 5000, Australia

[3]Mineral Sciences Department, Natural History Museum of Los Angeles County, 900 Exposition Boulevard, Los Angeles, CA 90007, U.S.A.

*E-mail: peter.elliott@adelaide.edu.au

ABSTRACT

Puttapaite, $Pb_2Mn^{2+}{}_2ZnCr^{3+}{}_4O_2(AsO_4)_4(OH)_6 \cdot 12H_2O$, is a new mineral from the Beltana deposit, Puttapa, Flinders Ranges, South Australia, Australia. It forms rosette-like aggregates to 50 μm across composed of diamond-shaped tablets to 45 μm in length and 5 μm in thickness. Crystals are flattened on {001} and the observed forms are {001} and {110}. The calculated density is 3.562 g/cm^{-3}. Optically, Puttapaite is biaxial (−) with $\alpha = 1.700(5)$, $\beta = 1.720(5)$, $\gamma = 1.730(5)$ and 2V (meas.) = 67(1)º. Electron microprobe analyses gave the empirical formula (based on 36 oxygen atoms *pfu*) $Pb_{1.96}(Mn^{2+}{}_{1.52}Ca_{0.28}Sr_{0.22})_{\Sigma 2.02}(Zn_{0.40}Mg_{0.39}Cu_{0.15})_{\Sigma 0.94}(Cr^{3+}{}_{2.89}Al_{0.45}Fe^{3+}{}_{0.40},Mn^{3+}{}_{0.26})_{\Sigma 4.00}O_2[(AsO_4)_{3.71}(Cr^{6+}O_4)_{0.29}]_{\Sigma 4.00}(OH)_{6.13} \cdot 11.87H_2O$. Puttapaite is monoclinic, $C2/m$, with $a = 12.405(3)$, $b = 10.565(2)$, $c = 12.311(3)$ Å, $\beta = 106.06(3)$º, $V = 1550.4(6)$ Å^3 and $Z = 2$. The structure was solved using synchrotron single-crystal x-ray diffraction data and refined to $R_1 = 0.1189$ on the basis of 915 observed reflections with $F_0 > 4\sigma(F_0)$. Puttapaite has a unique structure that consists of M_4O_{16} clusters that share corners with TO_4 tetrahedra, which in turn share corners with $M1$ octahedra in the [010] direction.

This is a 'preproof' accepted article for Mineralogical Magazine. This version may be subject to change during the production process.
DOI: 10.1180/mgm.2024.60

Clusters link in the [001] direction *via* corner sharing *M*2 octahedra to form sheets parallel to {100}. Pb anions lie between the sheets.

Keywords: puttapaite**,** new mineral species, lead manganese zinc chromium arsenate, crystal structure, synchrotron, Beltana deposit, Australia

INTRODUCTION

The Beltana deposit, near Puttapa, is the largest of several willemite ore bodies discovered in the Flinders Ranges of South Australia in the late 1960s. Geochemical stream sediment sampling within Lower Cambrian sediments detected anomalies for lead (40 ppm to 400 ppm) and zinc (100 to 1300 ppm). Subsequent rock sampling and detailed mapping led to the discovery of outcrops of willemite at Beltana, Aroona and Third Plain (Johns, 1972). Diamond drilling at Beltana located one major and several minor orebodies. Mining by opencut methods commenced in February 1974 and continued intermittently until 2003 (Emselle, 2005). From a mineralogical point of view, the Beltana deposit is the most interesting. The willemite orebody is associated with hematite alteration, is characterized by the total absence of sulphides and contains high levels of arsenic (0.5 wt %), lead (0.4–2.5 wt%) and manganese (Groves et al., 2003). Most of the arsenic and lead in the willemite ore are hosted in the mineral hedyphane, $Ca_2Pb_3(AsO_4)_3Cl$ (Brugger *et al*., 2003). Supergene alteration has resulted in the formation of a suite of arsenate and vanadate minerals, such as adamite, austinite, mimetite, tsumcorite, descloizite (Elliott *et al*., 1988; Elliott, 1991) and puttapaite**,** the last of which is the subject of this paper.

Puttapaite was collected from ore stockpiles in the 1990s and was at the time recognized as a probable new mineral species based on the unique chemistry. The size and nature of the crystals, which occur as rosette-like aggregates composed of many individuals, has made structural characterization difficult. The new mineral is named for the locality. The mineral and its name have been approved by the International Mineralogical Association Commission on New Minerals, Nomenclature and Classification (IMA2020-025). The

holotype specimen has been deposited in the in the South Australian Museum, Adelaide, South Australia, (Registration number G34869).

OCCURRENCE

The Beltana deposit is a high-grade hypogene willemite deposit hosted in Lower Cambrian carbonate rocks in the northern Flinders Ranges (Groves *et al*. 2003; Brugger *et al*. 2003). The willemite occurs as a replacement of dolomitized and hematitized Ajax Limestone of Lower Cambrian age. Mineralization is structurally controlled and associated with brecciation and extensive hematite-rich hydrothermal zincian dolomitization. The texture of the willemite is heterogeneous, resulting from various depositional mechanisms: direct replacement of carbonate host rock, open-space filling, internal sedimentation and brecciation. Acidic ore fluids corroded the host carbonate units and created open space by means of hydrothermal karsting and subsequent deposition of internal willemite sediment. Late-stage gangue minerals include Mn-rich calcite, dolomite, and minor quartz. On the periphery of the deposit, smithsonite formed by weathering of willemite. Using numerical geochemical modelling, Brugger *et al.* (2003) were able to show that willemite will precipitate at temperatures above 120º C as a result of water-rock interaction and fluid mixing processes. The mineralizing fluids carried large quantities of oxidized arsenic, as demonstrated by the large amounts of hedyphane in the deposit. The presence of arsenate in the hydrothermal fluids is likely to have inhibited the oxidation of sulphate to sulphide and resulted in the stabilization and precipitation of willemite rather than sphalerite and galena. Secondary arsenate minerals have formed in cavities in the willemite as a result of supergene alteration. A detailed description of the mineralogy is given by Elliott (1991). The new mineral occurs in vugs in a matrix composed of willemite and hematite. Associated minerals are rhodochrosite, hedyphane and adamite.

APPEARANCE AND PHYSICAL PROPERTIES

Puttapaite occurs as diamond-shaped tablets in rosette-like aggregates to 50 μm across (Figs. 1 and 2). Individual tablets are up to 45 μm in length and 5 μm in thickness. Crystals are flattened on {001} and the observed forms are {001} and {110} (Fig. 3). The

https://doi.org/10.1180/mgm.2024.60 Published online by Cambridge University Press

colour is pale green with a pale-green streak and a vitreous lustre. The tenacity is brittle, no cleavage was observed, and the fracture is splintery. Due to the small size of the crystals, the Mohs hardness could not be measured. A density of 3.562 g/cm^{-3} was calculated using the empirical chemical formula and unit-cell parameters from single-crystal data. Puttapaite is optically biaxial (–) with $\alpha = 1.700(5)$, $\beta = 1.720(5)$ and $\gamma = 1.730(5)$ (measured in white light). The 2V, measured on a spindle stage, using extinction data analyzed with the program EXCALIBR (Gunter *et al.* 2004) is 67(1)º; the calculated 2V is 69.8º. Dispersion could not be observed. Crystals are pleochroic with *X* light blue gray, *Y* colourless, *Z* not observed; $X > Y$. The Gladstone–Dale compatibility, $1 - (K_P/K_C)$, (Mandarino, 2007) is 0.047 (good) using the empirical formula and the unit-cell parameters determined from single-crystal data.

CHEMICAL COMPOSITION

Chemical data (ten spot analyses) were obtained using a Cameca SXFive electron microprobe (wavelength dispersive spectroscopy mode, acceleration voltage of 20 kV, a beam current of 20 nA and a 5 μm beam diameter). Raw X-ray intensities were corrected for matrix effects with a $\phi(\rho Z)$ algorithm (Pouchou and Pichoir, 1991). Both the crystal structure and infrared spectroscopy data confirm the presence of H_2O. Analytical data are given in Table 1. The empirical formula for puttapaite, calculated on the basis of 36 oxygen atoms, is $Pb_{1.96}(Mn^{2+}_{1.52}Ca_{0.28}Sr_{0.22})_{\Sigma 2.02}(Zn_{0.40}Mg_{0.39}Cu_{0.15})_{\Sigma 0.94}(Cr^{3+}_{2.89}Al_{0.45}Fe^{3+}_{0.40},Mn^{3+}_{0.26})_{\Sigma 4.00}O_2[(AsO_4)_{3.71}(Cr^{6+}O_4)_{0.29}]_{\Sigma 4.00}(OH)_{6.13}\cdot 11.87H_2O$. The ideal formula is $Pb_2Mn^{2+}_2ZnCr^{3+}_4O_2(AsO_4)_4(OH)_6\cdot 12H_2O$, which requires PbO 26.20, MnO 8.33, ZnO 4.78, Cr_2O_3 17.84, As_2O_5 26.98, H_2O 15.87, total 100 wt.%.

INFRA RED SPECTROSCOPY

The infrared-absorption spectrum of powdered puttapaite, recorded using a Nicolet 5700 FTIR spectrometer equipped with a Nicolet Continuμm IR microscope and a diamond-anvil cell in the range 650–4000 cm^{-1}, is shown in Fig. 4. A broad band in the O-H stretching region, with three sharp peaks at 3506, 3359 and 3149 cm^{-1}, can be attributed to the presence of H_2O and OH groups in the structure. Using the correlation of

https://doi.org/10.1180/mgm.2024.60 Published online by Cambridge University Press

Libowitzky (1999), the inferred O···O (donor–acceptor) distances are 2.90, 2.77 and 2.69 Å, which correspond to weak- to medium-strength hydrogen bonds. A band at 1651 cm^{-1} is assigned to the *v*2 (δ) H_2O bending mode. Bands at 850, 812 and 791cm^{-1} may be assigned to ν_3 vibrations of the AsO_4 tetrahedra.

CRYSTALLOGRAPHY

Powder X-ray diffraction

Powder X-ray diffraction data for puttapaite were obtained using a Rigaku R-AXIS Rapid II curved-imaging-plate microdiffractometer, with monochromatised Mo*K*α radiation (50 kV, 40 mA). A Gandolfi-like motion on the φ and ω axes was used to randomize the sample. Observed *d* values and intensities were derived by profile fitting using JADE Pro software (Materials Data, Inc.). Data (in Å for Mo*Kα*) are given in Table 2. Unit-cell parameters refined from the powder data using JADE Pro with whole-pattern fitting are a = 12.480(5), b = 10.588(5), c = 12.297(5) Å, β = 106.434(14)º, V = 1558.5(12) $Å^3$ and Z = 2.

Single-crystal X-ray diffraction

A single-crystal data collection was made at the macromolecular beam line MX2 of the Australian Synchrotron (Aragao *et al.*, 2018). Data were collected using a Dectris EigerX 16M detector and monochromatic radiation with a wavelength of 0.710760 Å. The data set was processed using XDS (Kabsch, 2010) without scaling, and with absorption correction and scaling using SADABS (Bruker, 2001). Data collection details are given in Table 3.

Structure determination

Structure solution in space group *C*2/m was carried out using SHELXT (Sheldrick, 2015a) and the structure was fined using SHELXL-2018 (Sheldrick, 2015b) as implemented in the WinGX suite (Farrugia, 1999). It was impossible to separate a high-quality individual from the rosette-like intergrowths. The best fragment found exhibited high mosaicity and multiple diffraction spots. As a result, relatively high R_{int} and final R values were obtained, 17.3% and 11.89%, respectively. We were unable to

https://doi.org/10.1180/mgm.2024.60 Published online by Cambridge University Press

locate the H atom positions in difference Fourier maps. Final atom coordinates and anisotropic-displacement parameters are listed in Table 4, selected interatomic distances and are given in Table 5, and bond-valence values, calculated using the parameters of Gagné and Hawthorne (2015) are given in Table 6.

Assignment of cation site-populations to the *M* sites and *T* site was completed based on observed mean bond lengths (Table 7). Mn^{2+} plus minor Ca and Sr were assigned to the larger *M*1 site, Zn, Mg plus minor Cu were assigned to the medium-sized *M*2 site and Cr^{3+} plus minor Al, Fe^{3+} and Mn^{3+} were assigned to the smaller *M*3 and *M*4 sites. Chemical analysis shows more Cr than is required to fill the *M*3 and *M*4 sites and insufficient As to fill the *T* site, hence 0.29 *apfu* Cr^{6+} was assigned to the *T* site. This assignment is supported by the <*T*–O> distance of 1.671 Å (Table 4), which is less than the distance expected for full occupancy by As^{5+} of 1.687 Å (Gagné and Hawthorne, 2018).

Structure description

The Pb site is [10]-coordinated (Fig. 5) with three short bonds to O2 and O5, three medium length bonds to OH6 and OW10 and four very long bonds to O4. The site exhibits one-sided coordination typical of Pb^{2+} with a stereochemically active $6s^2$ lone-electron-pair. Chemical analysis shows that the site is fully occupied by Pb. The *M* sites are each [6]-coordinated by O^{2-} anions, OH groups and H_2O groups in regular octahedral arrangements. The As site is coordinated as a regular tetrahedron by four O^{2-} anions and shows only slight distortions [angular range 107.1(8)–111.6(10) Å].

Two *M*3 and two *M*4 octahedra share edges to form a M_4O_{16} tetrameric cluster. Four TO_4 tetrahedra share O3 and O4 anions with each M_4O_{16} cluster to form a $M_4T_4O_{24}$ cluster. *M*1 octahedra link to TO_4 tetrahedra *via* corner sharing to link clusters in the [010] direction and *M*2 octahedra link to *M*4 octahedra *via* corner sharing to link clusters in the [001] direction to form sheets parallel to {100}. Sheets link in the [100] direction byPb-O bonds. The structure is shown in Figs. 6 and 7.

The structure contains four H_2O molecules and two OH groups. Although the H atoms could not be located during the refinement, a possible hydrogen bonding scheme based on O···O bond distances is summarized in Table 5. Under this scheme, the

https://doi.org/10.1180/mgm.2024.60 Published online by Cambridge University Press

underbonded O1, O2, O3 and O4 anions are receptors of hydrogen bonds as are each of the H_2O molecules. The observed O···O distances range from ~2.7 to ~3.3 Å indicating strong to very weak hydrogen bonds.

RELATIONSHIP TO OTHER MINERALS

Puttapaite represents a unique chemistry and structure type for minerals and inorganic compounds. There are many arsenate minerals that contain Pb and Zn and five arsenate minerals that contain Pb and Mn. Besides puttapaite, there is only one other arsenate mineral that contains Pb and Cr, fornacite. In fornacite, Cr is hexavalent whereas in puttapaite Cr is trivalent. The crystal structures of anthoinite, $AlWO_3(OH)_3$, (Grey *et al*. 2010) and bamfordite, $Fe^{3+}Mo_2O_6(OH)_3 \cdot H_2O$, (Birch et al. 1998) contain M_4O_{16} tetrameric clusters of edge-sharing octahedra and they have a similar layer structure. In the anthoinite structure there are two types of tetramer that share octahedral vertices with four adjacent tetramers to form stepped layers parallel to (001). Connectivity between layers is by hydrogen bonding. In the bamfordite structure, tetramers interconnect via octahedral dimers, $Fe^{3+}_2(O,OH,H_2O)_{10}$, to form stepped layers parallel to (100). The layers are linked by hydrogen bonding.

ACKNOWLEDGMENTS

The authors thank Ben Wade of Adelaide Microscopy, The University of Adelaide for assistance with the microprobe analysis. The infrared spectrum was acquired with the assistance of the Forensic Science Centre, Adelaide. This research was undertaken in part using the MX2 beamline at the Australian Synchrotron, part of ANSTO, and made use of the Australian Cancer Research Foundation (ACRF) detector. The authors thank two anonymous reviewers and Structures Editor Peter Leverett for their comments and corrections.

REFERENCES

Aragao, D., Aishima, J., Cherukuvada, H., Clarken, R., Clift, M., Cowieson, N.P., Ericsson, D.J., Gee, C.L., Macedo, S., Mudie, N., Panjikar, S., Price, J.R., Riboldi-

https://doi.org/10.1180/mgm.2024.60 Published online by Cambridge University Press

Tunnicliffe, A., Rostan, R., Williamson, R. and Caradoc-Davies, T.T. (2018) MX2: a high-flux undulator microfocus beamline serving both the chemical and macromolecular crystallography communities at the Australian Synchrotron. *Journal of Synchrotron Radiation*, **25**, 885–891.

Birch, W.D., Pring, A., McBriar, E.M., Gatehouse, B.M., and McCammon, C.A. (1998) Bamfordite, $Fe^{3+}Mo_2O_6(OH)_3 \cdot H_2O$, a new hydrated iron molybdenum oxyhydroxide from Queensland, Australia: Description and crystal chemistry. *American Mineralogist*, **83**, 172–177.

Brugger, J., McPhail, D.C., Wallace, M. and Waters, J. (2003) Formation of willemite in hydrothermal environments. *Economic Geology*, **98**, 819-835.

Bruker (2001) SADABS. Bruker AXS Inc., Madison, Wisconsin, USA.

Elliott, P., Pring, A. and Birch, W. D. (1988), Tsumcorite from Puttapa, South Australia. *Australian Mineralogist*, **3**, 67-69.

Elliott, P. (1991), Minerals from the Beltana mine, Puttapa, South Australia. *Mineralogical Record*, **22**, 449-456.

Emselle, N., McPhail, D.C. and Welch, S.A. (2005) Reliance, Flinders Ranges: mineralogy, geochemistry and zinc dispersion around a nonsulfide orebody. In C. Roach, Ed., Regolith 2005 ten tears of CRC LEME: proceedings of the CRC LEME Regional Regolith Symposia, p. 86-90. Cooperative Research Centre for Landscape Environments and Mineral Exploration, Australia.

Farrugia, L.J. (2012) *WinGX* and *ORTEP* for *Windows*: an update. *Journal of Applied Crystallography*, **45**, 849–854.

Gagné, O.C. and Hawthorne, F.C. (2015) Comprehensive derivation of bond-valence parameters for ion pairs involving oxygen. *Acta Crystallographica*, **B71**, 562–578.

Gagné O.C. and Hawthorne F.C. (2018) Bond-length distributions for ions bonded to oxygen: metalloids and post-transition metals. *Acta Crystallographica*, **B74**, 63–78.

Grey, I.E., Madsen, I.C., Mills, S.J., Hatert, F., Paterson, V. and Bastow, T.J. (2010) A new type of cubic-stacked layer structure in anthoinite, $AlWO_3(OH)_3$. *American Mineralogist*, **95**, 639–645.

https://doi.org/10.1180/mgm.2024.60 Published online by Cambridge University Press

Groves, I. M., Carman, C. E. and Dunlap, W. J. (2003) Geology of the Beltana willemite deposit, Flinders Ranges, South Australia. *Economic Geology*, **8**, 797-818.

Gunter, M.E., Bandli, B.R., Bloss, F.D., Evans, S.H., Su, S.C. and Weaver, R. (2004) Results from a McCrone spindle stage short course, a new version of EXCALIBR, and how to build a spindle stage. *The Microscope* **52**, 23–39.

Johns, R.K. (1972) Base metal occurrences with lower Cambrian sediments of the Northern Flinders Ranges. - Geol. Geological Survey of South Australia. Report of Investigations, 37.

Kabsch, W. (2010) XDS. *Acta Crystallographica*, **D66**, 125–132.

Libowitzky, E. (1999) Correlation of O-H stretching frequencies and O-H···O hydrogen bond lengths in minerals. *Monatshefte für Chemie*, **130**, 1047–1059.

Mandarino J.A. (2007) The Gladstone-Dale compatibility of minerals and its use for selecting mineral species for further study. *The Canadian Mineralogist*, 45, 1307–1324.

Pouchou, J.-L., and Pichoir, F. (1991) Quantitative analysis of homogeneous or stratified microvolumes applying the model "PAP". In K.F.J. Heinrich and D.E. Newbury, Eds., Electron Probe Quantitation, p. 31–75. Plenum Press, New York.

Sheldrick, G.M. (2015a) SHELXT - Integrated space-group and crystal-structure determination. *Acta Crystallographica*, **A71**, 3–8.

Sheldrick, G.M. (2015b) Crystal structure refinement with SHELXL. *Acta Crystallographica*, **C71**, 3–8.

https://doi.org/10.1180/mgm.2024.60 Published online by Cambridge University Press

FIGURE CAPTIONS

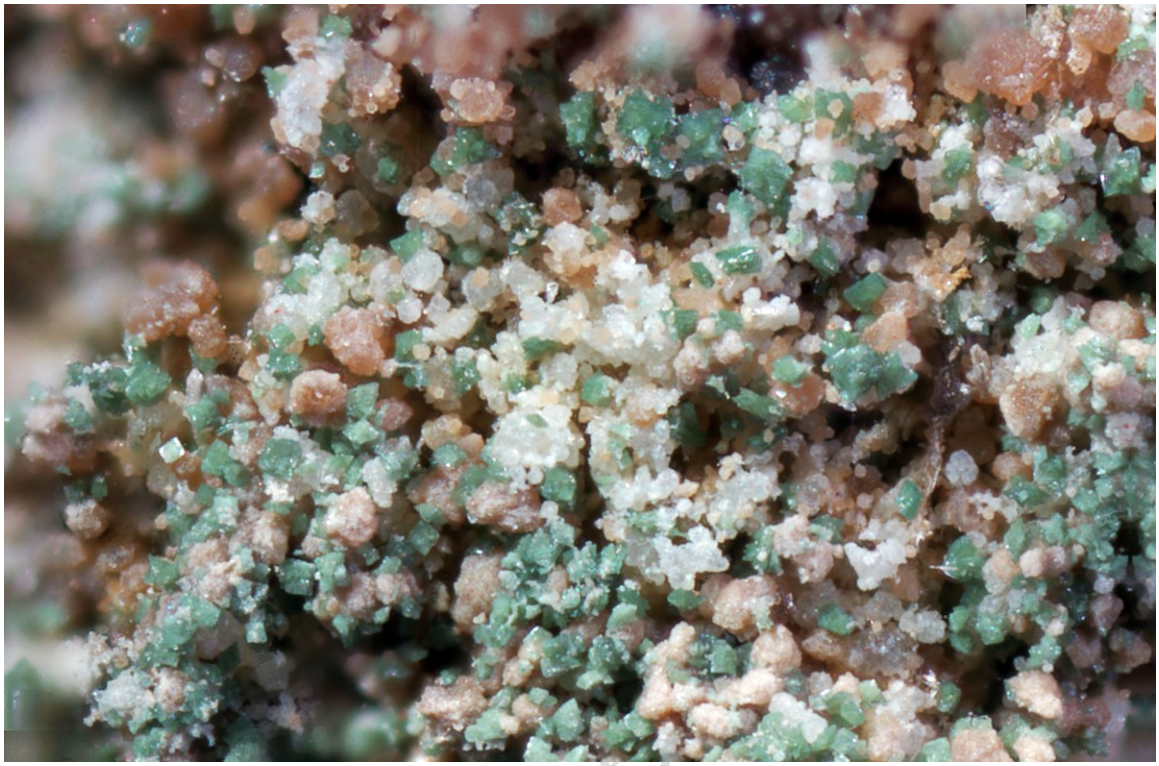

Figure 1. Pale-green crystals of puttapaite associated with smithsonite (orange brown) and willemite (white). The scale bar is 100 μm.

https://doi.org/10.1180/mgm.2024.60 Published online by Cambridge University Press

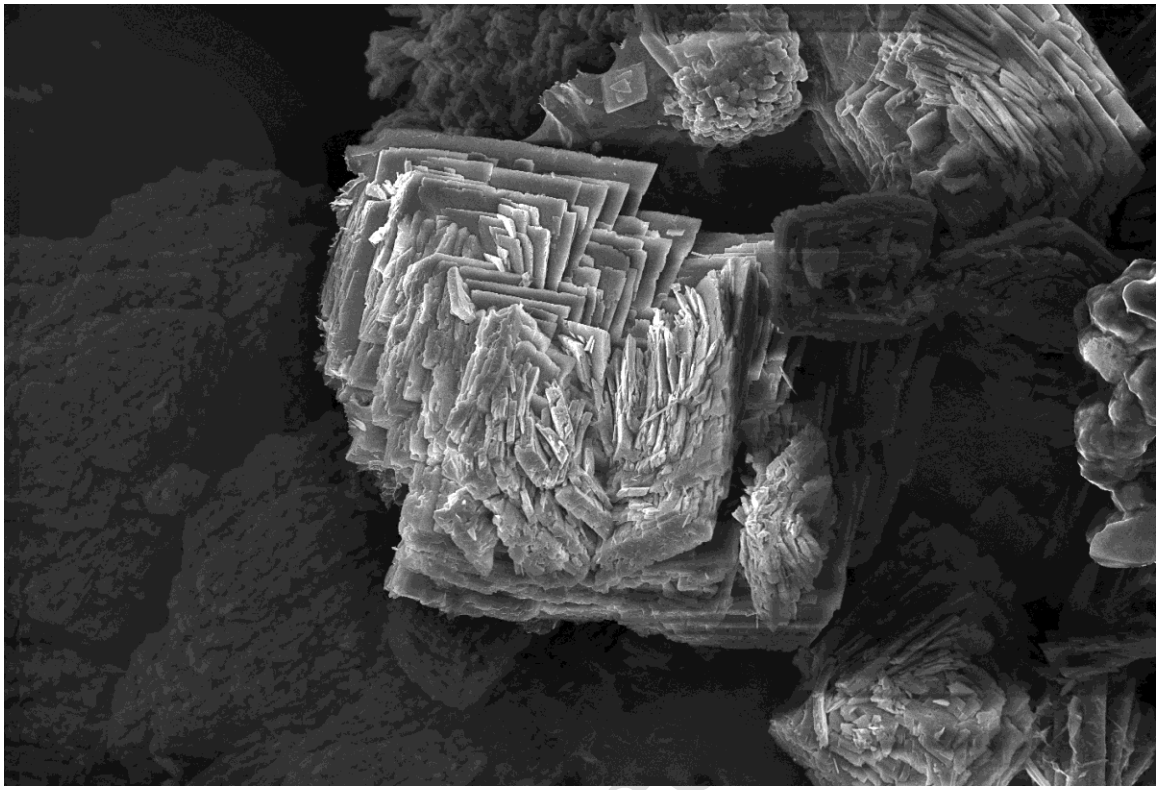

Figure 2. SEM photomicrograph showing crystals of puttapaite. The field of view is 0.3 mm.

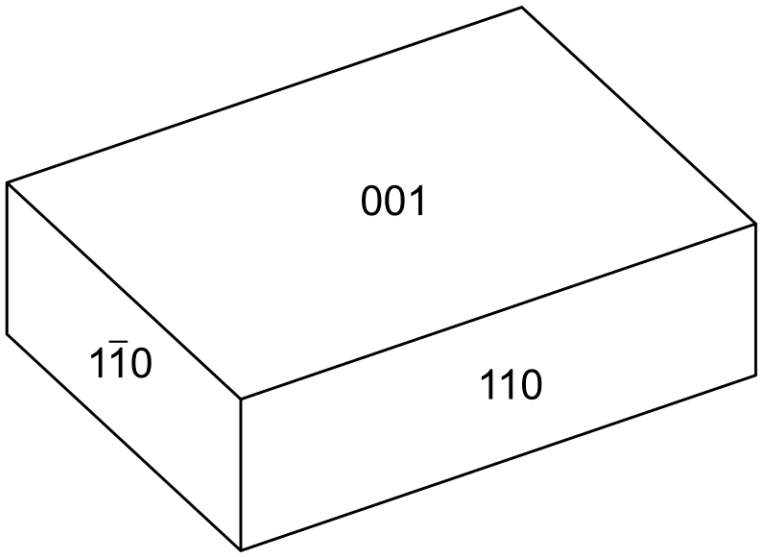

Figure 3. Crystal drawing of puttapaite; clinographic projection in standard orientation.

https://doi.org/10.1180/mgm.2024.60 Published online by Cambridge University Press

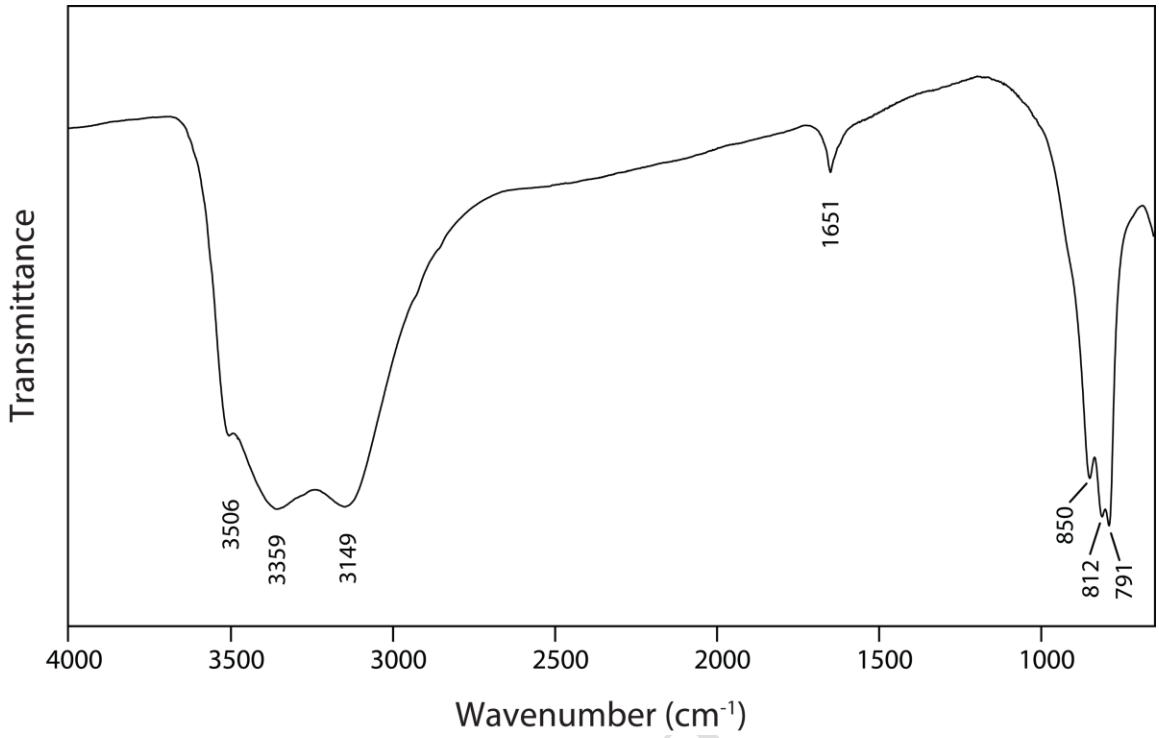

Figure 4. The FT-IR spectrum of powdered puttapaite.

https://doi.org/10.1180/mgm.2024.60 Published online by Cambridge University Press

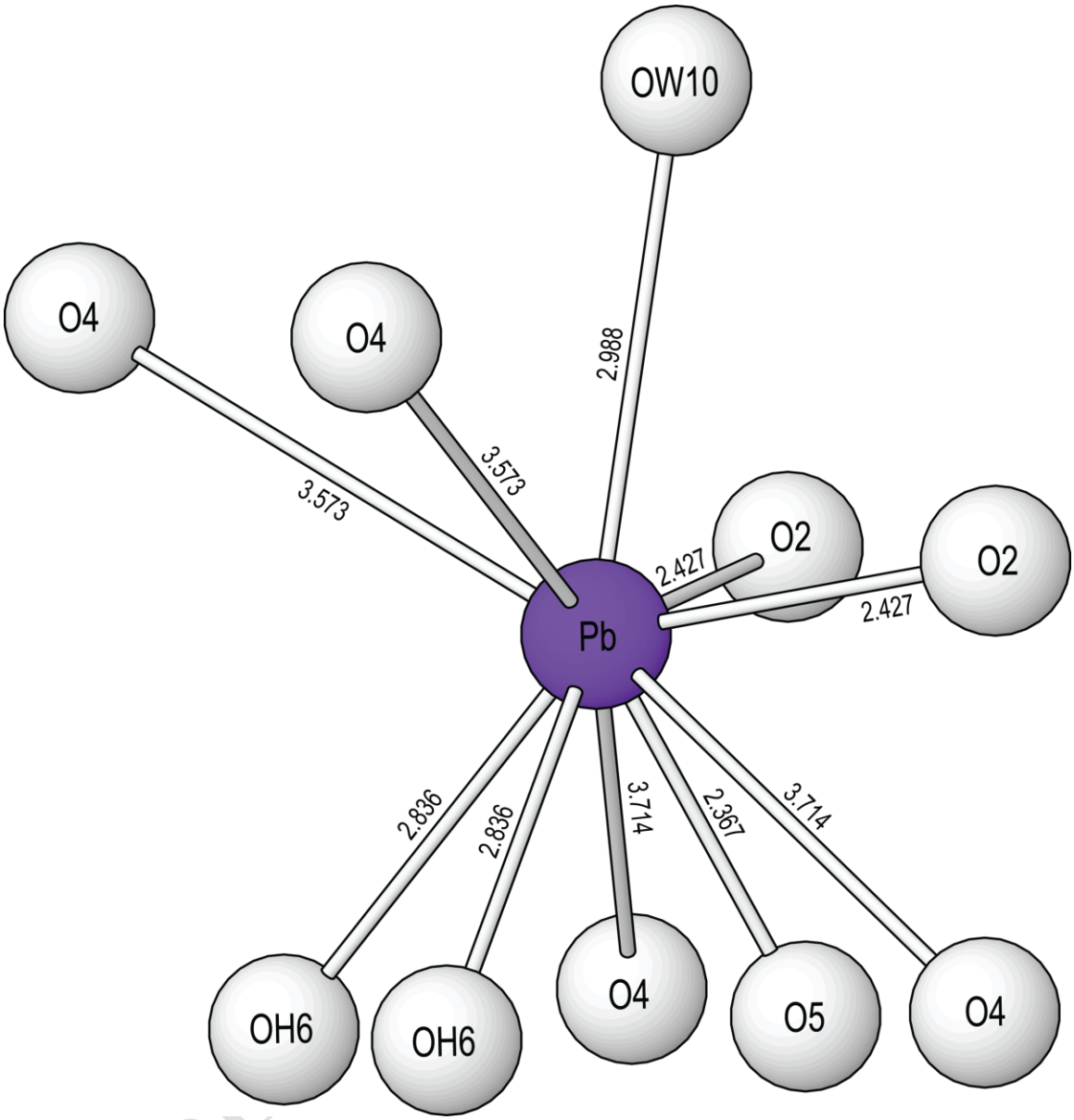

Figure 5. The Pb^{2+} coordination in puttapaite showing Pb-O bond lengths in angstroms, Å.

https://doi.org/10.1180/mgm.2024.60 Published online by Cambridge University Press

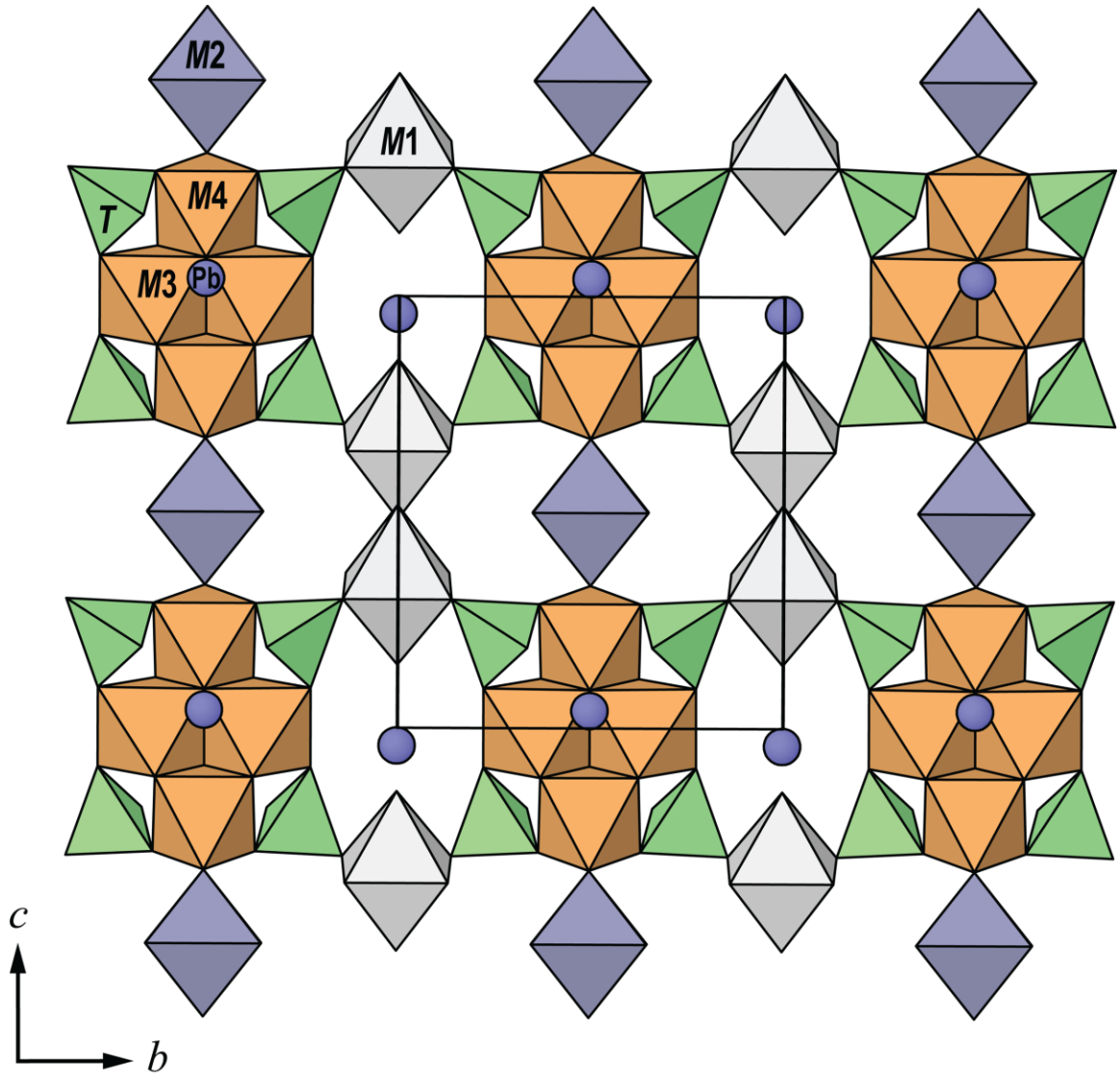

Figure 6. The crystal structure of puttapaite viewed along [100]. The unit cell is outlined.

https://doi.org/10.1180/mgm.2024.60 Published online by Cambridge University Press

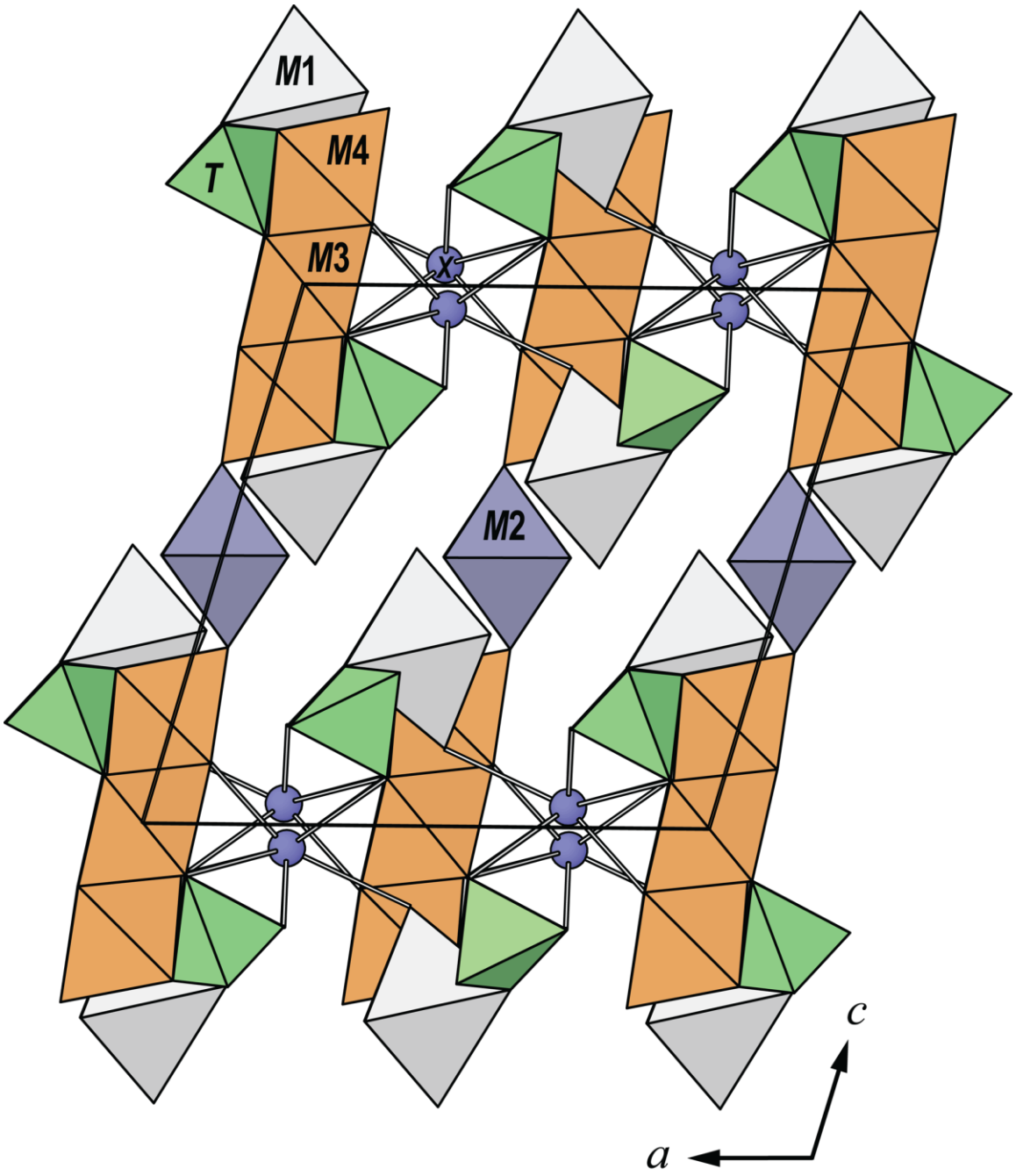

Figure 7. The crystal structure of puttapaite viewed along [010]. The unit cell is outlined.

Table 1. Analytical data for puttapaite.

Constituent	Wt.%	Range	Stand. Dev.	Probe Standard
PbO	26.20	25.59–27.18	0.51	galena

https://doi.org/10.1180/mgm.2024.60 Published online by Cambridge University Press

SrO	1.37	1.14–1.44	0.09	celestine
CaO	0.93	0.88–0.94	0.06	plagioclase
MnO*	6.48	5.47–7.38	0.68	rhodonite
Mn_2O_3*	1.21	0.31–2.11	0.61	rhodonite
ZnO	1.96	1.59–2.25	0.16	willemite
MgO	0.95	0.81–1.05	0.07	almandine-pyrope
CuO	0.70	0.59–0.77	0.06	chalcopyrite
Cr_2O_3**	13.17	12.21–13.97	0.57	Cr_2O_3
Fe_2O_3	1.90	1.71–1.99	0.09	almandine-pyrope
Al_2O_3	1.37	1.23–1.47	0.08	almandine-pyrope
As_2O_5	25.53	24.02–26.85	0.94	gallium arsenide
CrO_3**	1.74	0.74–3.08	0.71	Cr_2O_3
H_2O§	16.12			
Total	99.63			

*MnO and Mn_2O_3 calculated to give $Cr^{3+} + Al + Fe^{3+} + Mn^{3+} = 4.00$
**Cr_2O_3 and CrO_3 calculated to give $AsO_4 + Cr^{6+}O_4 = 4.00$
§calculated from the refined formula

Table 2. Powder X-ray diffraction data for puttapaite.

I_{obs}	d_{obs}	d_{calc}	I_{calc}	*hkl*
100	11.74	11.8305	100	0 0 1
23	7.88	7.9067	14	1 1 0
19	7.23	7.2136	10	-1 1 1
		6.0361	1	-2 0 1
15	5.961	5.9604	6	2 0 0
40	5.223	5.2825	6	0 2 0
		5.2179	15	-1 1 2
		4.8235	3	0 2 1
48	4.797	4.8147	24	2 0 1
13	4.352	4.3676	6	1 1 2
44	3.958	3.9752	16	-2 2 1
		3.9401	18	0 2 2
13	3.885	3.8094	4	-2 0 3
9	3.756	3.7193	5	3 1 0
71	3.605	3.6068	42	-2 2 2
		3.5584	2	2 2 1
		3.3774	1	1 3 0
		3.3170	1	-1 3 1
		3.3112	3	3 1 1
10	3.286	3.2957	5	1 1 3
17	2.618	2.6205	5	-4 2 2
		2.5956	3	4 2 0
17	2.560	2.5778	3	0 4 1
		2.5664	7	2 2 3
13	2.461	2.4713	5	1 3 3
		2.4683	3	-4 0 4
		2.4570	1	-4 2 3
11	2.407	2.4197	1	-2 4 1
		2.4148	3	2 4 0
		2.4119	2	3 1 3
		2.4045	1	-3 3 3
10	2.386	2.3983	1	2 0 4
		2.3905	4	-1 1 5
		2.3289	1	-2 4 2
20	2.309	2.3157	9	2 4 1
		2.2921	1	-5 1 3
		2.2583	1	3 3 2
12	2.168	2.1760	2	-3 3 4
		2.1705	2	-2 4 3
		2.1680	2	-4 0 5
15	1.8745	1.8837	1	2 2 5
		1.8803	1	-6 2 3
		1.8787	3	5 3 1
		1.8702	1	1 3 5
		1.8596	1	6 2 0
		1.8357	1	1 1 6
20	1.7964	1.8097	2	3 3 4
		1.8046	1	1 5 3
		1.8034	2	-4 4 4
		1.7980	1	-6 2 4
		1.7967	1	3 1 5
		1.7935	1	-2 4 5
		1.7918	1	-4 2 6
		1.7839	1	-6 0 5
14	1.7510	1.7608	1	0 6 0
		1.7557	3	-5 1 6
		1.7527	1	4 2 4
		1.7435	1	6 0 2
		1.7416	1	0 6 1
		1.7317	1	-7 1 1

https://doi.org/10.1180/mgm.2024.60 Published online by Cambridge University Press

18	3.132	3.1601	6	0 2 3
		3.1421	3	-3 1 3
13	3.069	3.1002	1	-4 0 1
		3.0898	8	-2 2 3
20	3.013	3.0393	9	2 2 2
		3.0181	2	-4 0 2
		3.0004	2	-2 0 4
		2.9802	4	4 0 0
17	2.941	2.9576	4	0 0 4
		2.9537	5	-1 1 4
7	2.837	2.8387	4	1 3 2
		2.8351	2	3 1 2
10	2.794	2.7755	5	-4 0 3
32	2.686	2.7173	5	4 0 1
		2.6789	2	-3 3 1
		2.6738	12	-4 2 1
		2.6707	2	-1 3 3
17	2.649	2.6413	4	0 4 0
		2.6356	2	3 3 0
15	2.140	2.1605	2	1 1 5
		2.1528	4	2 4 2
		2.1433	3	1 3 4
		2.1284	1	-5 1 4
5	2.049	2.0686	3	3 1 4
		2.0325	1	1 5 1
11	2.015	2.0134	2	-1 3 5
		2.0120	2	-6 0 3
		2.0057	1	-4 2 5
		2.0013	1	-1 1 6
12	1.9846	1.9893	1	5 1 2
		1.9825	2	-2 4 4
		1.9767	1	4 4 0
		1.9700	1	0 4 4
		1.9637	1	2 4 3
7	1.9484	1.9472	1	-3 3 5
		1.9410	2	-5 1 5
10	1.9225	1.9337	1	1 5 2
		1.9147	3	-6 2 1
		1.8940	1	4 4 1
19	1.5984	1.7150	1	-3 1 7
		1.6901	2	-6 2 5
		1.6876	1	0 6 2
		1.6585	1	-2 6 2
		1.6500	1	4 4 3
		1.6261	1	-6 4 2
		1.6078	1	0 6 3
		1.6012	1	-1 5 5
		1.6005	3	-6 4 3
		1.5890	1	-5 3 6
		1.5809	1	3 1 6
16	1.5524	1.5673	1	-3 5 5
		1.5586	2	-3 3 7
		1.5501	1	-8 0 2
		1.5489	1	-6 4 4
		1.5421	1	-8 0 3
12	1.5231	1.5311	2	-4 6 1
		1.5297	1	6 4 1
		1.5209	1	-4 6 2
		1.5160	1	4 6 0
		1.5101	1	2 6 3

Table 3. Crystal data, data collection and refinement details.

Space group	C*2/m*
a,*b*,*c* (Å)	12.405(3), 10.565(2), 12.311(3)
β(º)	106.06(3)
V (Å^3), Z	1550.4(6), 2
F(000)	1382.0
μ (mm^{-1})	16.461
Absorption correction	multi-scan, T_{min} ,T_{max} = 0.209 0.436
Crystal dimensions (mm)	0.030 x 0.015 x 0.005
Diffractometer	Dectris EigerX 16M
Temperature (K)	100
Radiation	Synchrotron, λ = 0.710754 Å
Crystal detector distance (mm)	108.033
θ range (°)	1.721-27.124
h,*k*,*l* ranges	-15 → 15, -13 → 13, -15 → 15

https://doi.org/10.1180/mgm.2024.60 Published online by Cambridge University Press

Total reflections measured	9023
Unique reflections	1695 (R_{int} = 0.173)
$R1$ for $F_0 > 4\sigma(F_0)$.	11.89%
w$R2^{\dagger}$ for all F_0^2	34.41%
Reflections used $F_0^2 > 4\sigma(F_0^2)$	915
Number of parameters refined	130
GooF	1.123
$(\Delta/\sigma)_{max}$	0.000
$\Delta\rho_{max}$, $\Delta\rho_{min}$ (e/Å)	2.705, -1.953

$^{\dagger}wR2 = \Sigma w(|F_o|^2-|F_c|^2)^2 / \Sigma w|F_o|^2)^{1/2}$; w = $1/[\sigma^2(F_o^2) + (0.02\ P)^2]$; P = ([max of (0 or F_0^2)] + $2F_c^2$)/ 3

https://doi.org/10.1180/mgm.2024.60 Published online by Cambridge University Press

Table 4. Fractional atomic coordinates and displacement parameters (in Å^2) for puttapaite.

	x	y	z	U^{eq}	U^{11}	U^{22}	U^{33}	U^{12}	U^{13}	U^{23}
Pb	0.23676(13)	0	0.45939(12)	0.0817(8)	0.0828(11)	0.0757(11)	0.0914(11)	0	0.0324(8)	0
*M*1	0.6144(6)	0.5	0.8330(6)	0.078(3)	0.079(5)	0.071(4)	0.087(4)	0	0.027(3)	0
*M*2	0.5	0	1	0.073(4)	0.074(6)	0.079(7)	0.069(5)	0	0.023(4)	0
*M*3	0.5	0.1436(5)	0.5	0.073(2)	0.078(4)	0.068(3)	0.075(3)	0	0.021(2)	0
*M*4	0.5199(5)	0	0.7118(5)	0.075(2)	0.084(4)	0.070(4)	0.077(4)	0	0.030(3)	0
T	0.6905(2)	0.2331(3)	0.7166(2)	0.0772(12)	0.0779(19)	0.0734(18)	0.0811(18)	-0.0022(11)	0.0234(12)	-0.0021(13)
O1	0.7311(17)	0.3585(18)	0.7975(16)	0.097(6)	0.100(12)	0.074(11)	0.107(11)	-0.021(9)	0.011(9)	-0.019(10)
O2	0.7982(13)	0.1624(18)	0.6857(15)	0.087(5)	0.064(9)	0.089(12)	0.111(11)	0.005(9)	0.027(8)	0.000(9)
O3	0.6320(14)	0.1325(18)	0.7877(12)	0.087(5)	0.090(11)	0.094(12)	0.076(9)	-0.003(8)	0.018(8)	0.009(10)
O4	0.5982(16)	0.2759(16)	0.5918(12)	0.084(5)	0.098(12)	0.075(10)	0.078(8)	-0.012(7)	0.025(8)	-0.019(9)
O5	0.4088(18)	0	0.411(2)	0.081(6)	0.073(13)	0.089(15)	0.097(14)	0	0.050(11)	0
OH6	0.446(3)	0	0.830(2)	0.098(8)	0.12(2)	0.098(18)	0.085(14)	0	0.051(14)	0
OH7	0.4155(15)	0.1272(16)	0.6149(14)	0.082(4)	0.094(11)	0.066(9)	0.090(9)	0.007(7)	0.029(8)	-0.005(9)
OW8	0.666(3)	0.5	1.016(3)	0.134(12)	0.13(3)	0.15(3)	0.12(2)	0	0.023(19)	0
OW9	0.491(2)	0.634(3)	0.8597(18)	0.122(7)	0.128(17)	0.123(19)	0.112(14)	-0.014(13)	0.030(12)	0.018(15)
OW10	0.511(3)	0.5	0.646(3)	0.107(9)	0.11(2)	0.087(19)	0.13(2)	0	0.044(17)	0
OW11	0.611(2)	0.150(3)	0.9991(19)	0.125(8)	0.135(19)	0.135(19)	0.107(13)	0.000(13)	0.036(13)	0.003(17)

https://doi.org/10.1180/mgm.2024.60 Published online by Cambridge University Press

Table 5. Selected interatomic distances (Å) and possible hydrogen bonds (Å) for puttapaite.

Pb	O5	2.367(18)	*M*2	OH7	2.02(2)
	O2	2.427(19)		OH7	2.02(2)
	O2	2.427(19)		OW11	2.10(3)
	OH6	2.835(17)		OW11	2.10(3)
	OH6	2.835(17)		OW11	2.10(3)
	OW10	2.99(3)		OW11	2.10(3)
	O4	3.573(16)		<*M*–O>	2.07
	O4	3.573(16)			
	O4	3.715(19)	*M*3	OH6	1.988(16)
	O4	3.715(19)		OH6	1.988(16)
	<*X*–O>	3.045		O4	1.988(17)
				O4	1.988(17)
*M*1	OW8	2.17(4)		O5	2.022(17)
	OW9	2.17(2)		O5	2.022(17)
	OW9	2.17(2)		<*M*–O>	1.999
	O1	2.21(2)			
	O1	2.21(2)	*M*4	OH7	1.92(2)
	OW10	2.30(3)		O5	1.956(19)
	<*M*–O>	2.21		O3	2.012(19)
				O3	2.012(19)
T	O1	1.650(17)		OH6	2.013(18)
	O2	1.664(17)		OH6	2.013(18)
	O3	1.665(19)		<*M*–O>	1.988
	O4	1.705(18)			
	<*T*–O>	1.671			

Possible hydrogen bonds

OH6...O2	2.92	OW9...OW8	3.13
OH7...O1 x 2	2.99	OW9...OW11	2.99
OW8...O3 x 2	3.28	OW10...O4 x 2	2.76
OW8...OW9 x 2	3.130	OW11...O1	2.72
OW8...OW11 x 2	3.24	OW11...O3	2.69
OW9...O2	2.75	OW11...OW9	2.99
OW9...O3	3.28		

Table 6. Bond-valence analysis for puttapaite.

	Pb	*M*1	*M*2	*M*3	*M*4	*T*	Sum
O1		0.31 $^{x2}\downarrow$				1.37	1.69
O2	0.41 $^{x2}\downarrow$					1.32	1.73
O3					0.45 $^{x2}\downarrow$	1.32	1.77
O4	0.03 $^{x2}\downarrow$			0.48 $^{x2}\downarrow$		1.18	1.71

https://doi.org/10.1180/mgm.2024.60 Published online by Cambridge University Press

	0.02 x2↓					
O5	0.47			0.44 x2	0.53	1.88
OH6	0.16 x2↓			0.48 x2↓	0.45 x2↓	1.09
OH7			0.41 x2↓		0.58	0.99
OW8		0.35				0.35
OW9		0.35 x2				0.35
OW10	0.12	0.25				0.37
OW11			0.32 x4↓			0.32
Sum	1.83	1.91	2.11	2.79	2.91	5.18

Table 7. Refined site-scattering values (*epfu*) and assigned site-populations for puttapaite.

Site	Site scattering	Site population	Calculated site scattering	$<M–O>_{obs}$	$<M–O>_{calc}$
*M*1	21.50	$Mn^{2+}_{0.75}Ca_{0.14}Sr_{0.11}$	25.73	2.205	2.227
*M*2	18.00	$Zn_{0.43}Mg_{0.41}Cu_{0.16}$	22.46	2.073	2.012
*M*3	26.64	$Cr^{3+}_{0.72}Mn^{3+}_{0.07}Al_{0.11}Fe^{3+}_{0.10}$	23.06	1.975	1.971
*M*4	25.68	$Cr^{3+}_{0.72}Mn^{3+}_{0.07}Al_{0.11}Fe^{3+}_{0.10}$	23.06	1.988	1.976
T	33.86	$As_{0.93}Cr^{6+}_{0.07}$	32.37	1.671	1.680

https://doi.org/10.1180/mgm.2024.60 Published online by Cambridge University Press